Dental Materials 39 (2023) 568–576

Contents lists available at ScienceDirect

Dental Materials

journal homepage: www.elsevier.com/locate/dental

Fabrication of color-graded feldspathic dental prosthetics for aesthetic and restorative dentistry

Imam Akbar Sutejo[a,b], Jeehwan Kim[a,c], Sinuo Zhang[a,b], Chang Woo Gal[a], Yeong-Jin Choi[a], Honghyun Park[a], Hui-suk Yun[a,b,*]

[a] Korea Institute of Materials Science (KIMS), Changwon, Republic of Korea,
[b] University of Science and Technology (UST), Daejeon, Republic of Korea
[c] Pusan National University (PNU), Busan, Republic of Korea

ARTICLE INFO

Keywords:
Stereolithography
Functionally graded additive manufacturing
Dental crowns
Dental porcelain
Color-gradient

ABSTRACT

Objective: Feasibility investigation of natural teeth shades replication on dental prosthetics fabricated via functionally graded additive manufacturing (FGAM) using combination of feldspathic porcelain (FP) and yttrium aluminum garnet cerium ($Y_3Al_5O_{12}$:Ce, YAG:Ce) as a promising esthetic restoration option.
Methods: Color-graded feldspathic crown fabrication parameter through FGAM method was comprehensively examined from the slurry rheology, cure depth, debinding to sintering temperature. Effect of light absorbent also checked towards overcuring reaction during UV exposure by the shape comparison. Lastly, the flexural bending strength measured following ISO 6872:2015 to assure the applicability. Applying the studied parameter, natural teeth shades then imitated and investigated by alteration of FP and FP + 0.1 wt% YAG:Ce (Y-FP). Generated color across the structure captured through mobile camera, interpreted through the CIELAB coordinate and the gradation confirmed by the color differences (ΔE_{00}) calculated using CIEDE2000 formula.
Result: Parameter study indicated that 70 wt% of FP slurry with 3 wt% dispersant and 0.2 wt% light absorbent is favored. It produces excellent flowability in our FGAM system with less overcuring justified by edge margin reduction from 95.65° to 90.00° after UV exposure on rectangle shapes masking. The obtain structure also offers adequate flexural bending strength of 106.26 MPa (FP) and 101.36 MPa (Y-FP) after sintering at 780 °C. This validated the materials as class 2 dental prosthetics citing ISO 6872:2015. Color gradation was verified by the yellow b* value reduction (14.8 to −3.33) as it shifted from cervical to incisal area while ΔE_{00} further affirmed the differences from each segment in comparison with the FP and Y-FP.
Significance: Color gradation was successfully replicated by FP and YAG:Ce composition shift via FGAM technique. This result highlights the potential of FGAM as an alternative for fabricating dental prosthetics with high efficiency and improved esthetic appeal.

1. Introduction

The visual presentation of teeth is crucial due to the social impact [1,2]. This is particularly critical at the front of the mouth, where the incisors, canines, and premolar are frequently exposed [3–6]. Hence, ceramic crowns for dental restoration should incorporate shade gradation to match the natural teeth nearby.

Dental prosthetics today are often fabricated using computer-aided design/computer-aided manufacturing (CAD/CAM). Complex prosthetics could be produced by milling a block of material (subtractive manufacturing) [14]. The CAD/CAM technique eliminates some laborious steps, shortens the production time, and delivers consistent quality [15–18]. Unfortunately, damages are unavoidable when carving from a monolithic structure [17–19]. To improve the esthetics, a human expert can remove parts of the surface from the shaped block and apply personalized color in a staining-glazing approach (multi-layering treatment) [7–10]. Currently, there is also a trend of shifting from a single material to multilayer or multilayer pre-colored blocks [11–14] in order to eliminate the arduous staining process.

Additive manufacturing (AM) is another promising way to fabricate ceramic dental prosthetics [15–18]. Among the available AM techniques,

* Correspondence to: Department of Advanced Biomaterials Research, Ceramic Materials Division, Korea Institute of Materials Science (KIMS), 797 Changwon-daero, Seongsan-gu, Changwon-si, Gyeongsangnam-do 51508, Republic of Korea.
E-mail address: yuni@kims.re.kr (H.-s. Yun).

https://doi.org/10.1016/j.dental.2023.03.021
Received 3 January 2023; Received in revised form 22 March 2023; Accepted 31 March 2023

digital light processing (DLP) employs photosensitive resin as a ceramic carrier and cures it by UV light to form the prosthetic structure. Previous studies have addressed the usability, structural accuracy, and post-treatment crack formation mainly for single materials such as zirconia [19,20], alumina [21], and lithium disilicate glass [22]. Meanwhile, there are very few in-depth reports on manipulating the color of dental prosthetics fabricated using AM. In one study, multi-layering treatment was applied before the fabricated structure was sintered [23]. Another study explored the doping of Fe_2O_3 colorant in dental AM [24].

Here, we adopt functionally graded additive manufacturing (FGAM) to create customizable color gradation in ceramic dental prosthetics. The FGAM process not only refines the flexibility of AM to produce complex shapes but also allows gradation within the structure [25–27]. Here, "gradation" can mean material arrangement, distribution, dimension, or even composition to produce inhomogeneous properties in the same structure. When applied to the compositional gradation of coloring agents, FGAM has the potential to create custom color gradation in prosthetics, replacing the multilayer block fabrication and CAD/CAM technique mentioned earlier. However, several issues must be addressed when the AM system uses multiple components. Especially, when several components are combined, the mixture can behave differently during formation of the curing layer and/or exhibit different shrinkages post-treatment [26,30].

Feldspathic porcelain ($K_xNa_{1-x}AlSi_3O_8$, FP) is a traditional glass-based dental ceramic system [18,28]. FP provides great esthetics and translucency [29,30] due to its amorphous glassy phase [31], although its mechanical properties are inferior [28,32] compared to other ceramics such as zirconia [24,33]. The color of FP has been adjusted by adding transition metal ions such as Ce^{4+} [34,35], Tb^{3+} [36], Dy^{3+} [36], and Fe^{3+} [13,24,35]. On the other hand, yttrium aluminum garnet Cerium (YAG:Ce; $Y_3Al_5O_{12}$:Ce) is a material with lattice properties desirable for laser host [37]. But, it was also found that the processing temperature of YAG could be as low as 900 ˚C [38], which produces a yellowish luster [39]. Therefore, combining YAG:Ce and a white dental ceramic could reproduce both the translucency and tinted color of natural teeth. However, such in-depth studies have not been reported before. Generally, FP is the favored dental ceramic for anterior positions because it visually blends better with the neighboring teeth [31–33]. Plus, this area is not engaged in grinding motion [34] that would require zirconia with higher strength [35]. Another reason for choosing FP is that glass-based ceramics display better processability in DLP-based AM, while zirconia suffers from low cure depth [40] and overcuring [41].

The current study starts with our previously developed film-based DLP system [42,43] and modifies it for the FGAM process by introducing multiple cartridges to easily accommodate various materials. First, we establish the ideal composition in the feed slurry for fabricating dental crowns, based on the measured FP particle size, slurry viscosity, and feed transport flowability. We also strictly control the photocurability by using various additives to maximize the structural precision. Next, we examine the processing temperature, starting point of dimension reduction during heat treatment, final shrinkage, as well as flexural bending strength of the fabricated samples. We hypothesize that crowns with customizable color gradation could be fabricated by adjusting the ratio between YAG:Ce-added FP (Y-FP) and FP in different structural regions (cervical, middle, and incisal). As a translucent ceramic, FP should have a positive effect on the curing behavior and helps achieve smooth color transition.

2. Materials and methods

2.1. Materials

Powders of FP and Y-FP (HASS, Republic of Korea) were used as the base ceramic materials. The resin consisted of trimethylolpropane triacrylate (TMPTA) and poly(propylene glycol) diacrylate (PPGDA) (Sigma-Aldrich, USA). The photoinitiator (PI) was a combination of bis (2,4,6-trimethylbenzoyl)-phenylphosphineoxide (Irgacure 819) and 2,2-dimethoxy-1,2-diphenylethan-1-one (Irgacure 651) (BASF, Germany). Furthermore, we tested two additives DISPERBYK-180 (BYK180; Altana AG, Germany) and Remazol Brilliant Orange 3 R (RO16; Sigma-Aldrich, USA) to improve the homogeneity and control the curing behavior, respectively.

2.2. Preparation of ceramic slurry

TMPTA and PPGDA were mixed at a weight ratio of 1:1 and added with PI (0.01 wt% Irgacure 819 and 4 wt% Irgacure 651 of total resin). The mixture was homogeneously combined in a planetary centrifugal mixer (ARE-310, THINKY, USA) at 2000 rpm for 5 min. BYK-180, RO16, and FP or Y-FP powder were then added before mixing for another 5 min

2.3. Optimization of slurry composition

Before optimizing the slurry, we characterized the FP particle size with a laser particle size analyzer (LS I3 320, Beckman Coulter, USA) and the particle shape with a scanning electron microscope (SNE-4500M Plus, SEC, Korea). BYK180 (1–5 wt% to the powder) was used to enhance homogeneous distribution of FP particles in the resin, while the loading capacity of ceramic in the resin ranged from 40 to 70 wt%. The homogeneity and loading capacity were validated by measuring the rheological behavior using a TS rheometer (Discovery HR-1, TA Instruments, USA) in the flow sweep mode and shear rate of 1–100 s^{-1}.

2.4. Optimization of curing behavior

Curing behavior of the photocurable resin was measured with a UV-Vis spectrometer (Mega-900, SCINCO, Korea) in the wavelength range of 200–800 nm. The effect of RO16 (0.1–0.3 wt% of the resin) was measured as well. Using the optimized composition ratio (70 wt% solid loading, 3 wt% BYK180), we measured the cure depth under a rectangular shape mask and UV light irradiation (DLP UV specification, 405 nm, 8.5 mW/cm^2). After UV exposure for 1–10 s, the uncured slurry was cleaned off, the thickness of the cured part was measured, and a 60 × magnified image was taken using a video microscope system (SV-55, SOMETECH, Korea) to measure the edge angle.

2.5. Green body debinding, sintering, and product characterization

The UV-cured sample was washed with resin monomers to remove residual slurry and blown gently with an air gun. The obtained green body underwent debinding by heating at 1 ˚C/min to 650 ˚C, followed by soaking for 3 h at 300, 350, 400, and 650 ˚C to remove the resin. The subsequent sintering process involved heating at 1 ˚C/min to 300 ˚C, then at 5 ˚C/min to 780 ˚C, and finally holding for 3 h at 780 ˚C to densify the powder. Both heating steps were designed according to the material's thermal behavior (Fig. S3) characterized by thermogravimetry/differential scanning calorimetry (TG/DSC; SDT Q600, TA Instrument, USA). Finally, product shrinkage was measured by size reduction along the three axes, using the middle point as reference (origin point). Following ISO 6872:2015, the density was measured by the Archimedes method (XPE205, Mettler Toledo, Switzerland), and the flexural bending strength was assessed using a universal testing machine (UTM; RB-305 MICROLOAD, R&B, Korea).

2.6. Fabrication of color-graded crowns

Crown structures were fabricated using an in-house developed DLP system (Fig. S1). The crown 3D model had a maximum height of 11.6 mm, which was sliced into 580 2D layers with a thickness of 20 μm. We employed five compositions of the ceramic materials ranging from 100% Y-FP to 100% FP with 25% increments (Table 1).

Table 1
Five FP/Y-FP compositions and their adoption in the 580 layers in the crown model to create TYPE1–TYPE3 gradations.

Composition name	Composition mixture	Layers in the sliced 3D crown model			
	FP/Y-FP (%)	TYPE1	TYPE2	TYPE3	
FPY-100/0	100/0	511–580	466–580	401–580	Bottom → top
FPY-75/25	75/25	421–510	351–465	261–400	
FPY-50/50	50/50	321–420	236–350	161–260	
FPY-25/75	25/75	181–320	121–235	71–160	
FPY-0/100	0/100	1–180	1–120	1–70	

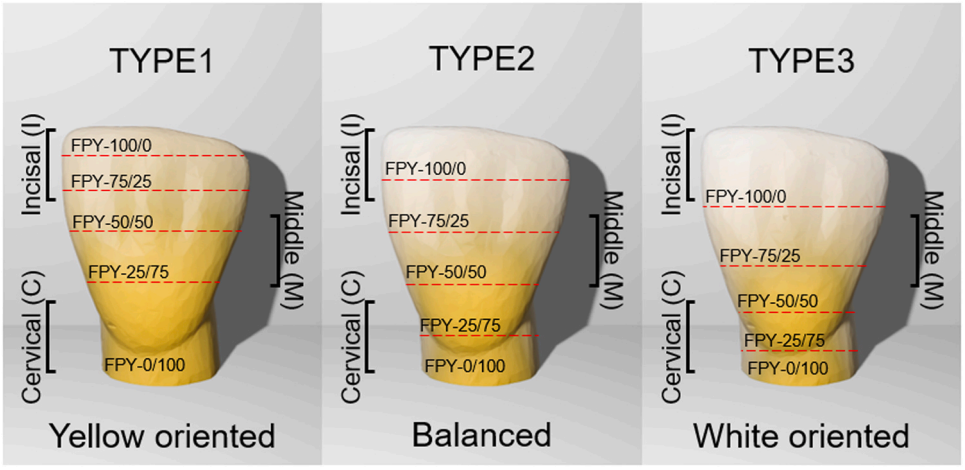

Fig. 1. - Three teeth models built from gradient segmentation.

The three color gradations are visually illustrated in Fig. 1. By using different ratios of Y-FP across the layers, we hope to achieve flexible color control throughout the model. Take TYPE1 as an example, the first (bottom) segment consists of 180 layers in a yellower shade (FPY-0/100), followed by three segments with decreasing yellow coloration (140 layers of FPY-25/75, 100 layers of FPY-50/50, and then 90 layers of FPY-75/25), and topped by a slightly whiter shade in the top segment (70 layers of FPY-100/0). In contrast, TYPE2 and TYPE3 had different layer arrangements to produce a more balanced and whiter color gradation, respectively.

2.7. Color analysis

After sintering, esthetics of the color-graded crowns was directly evaluated without any post-polishing nor glazing process. A mobile phone (SAMSUNG SM-S908N, Korea) was used to photograph the crown, and colors in the image were directly converted to the CIELAB coordinates (L*, a*, and b*). L* describes perceptual lightness (0 = black, 100 = white), while a* (green-red) and b* (blue-yellow) can take either positive or negative values. The color difference (ΔE_{00}) was then calculated according to CIEDE2000 [44].

3. Results

3.1. Particle size and slurry viscosity

Fig. 2 shows the characteristics of FP and Y-FP particles and rheological behaviors of the feed slurries. The FP and Y-FP particles are similar in their angular shapes and size distributions (D_{50} = 4.24 μm), as shown in Fig. 2a. Adding 1–3 wt% BYK180 significantly reduced the viscosity, whereas a higher amount (4 and 5 wt%) increased the viscosity to the level at 2 wt% addition (Fig. 2b). Next, the maximum solid loading in slurries containing 3 wt% BYK180 was determined to be 70 wt%, since a 75 wt% loading caused a spike in the viscosity (Fig. 2c). Therefore, our subsequent experiments used the optimal slurry composition of 3 wt% BYK180 and 70 wt% solid loading.

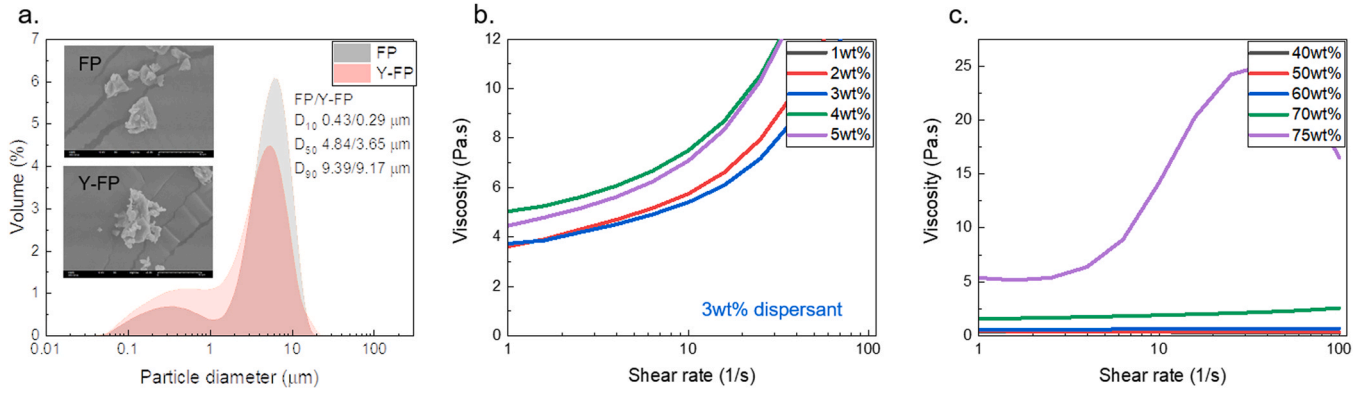

Fig. 2. - Characteristics of the feed slurry. (a) Shapes and size distribution of FP and Y-FP particles. (b) Viscosity of FP slurry with various amounts of BYK180. (c) Viscosity of FP slurry with increasing solid loading.

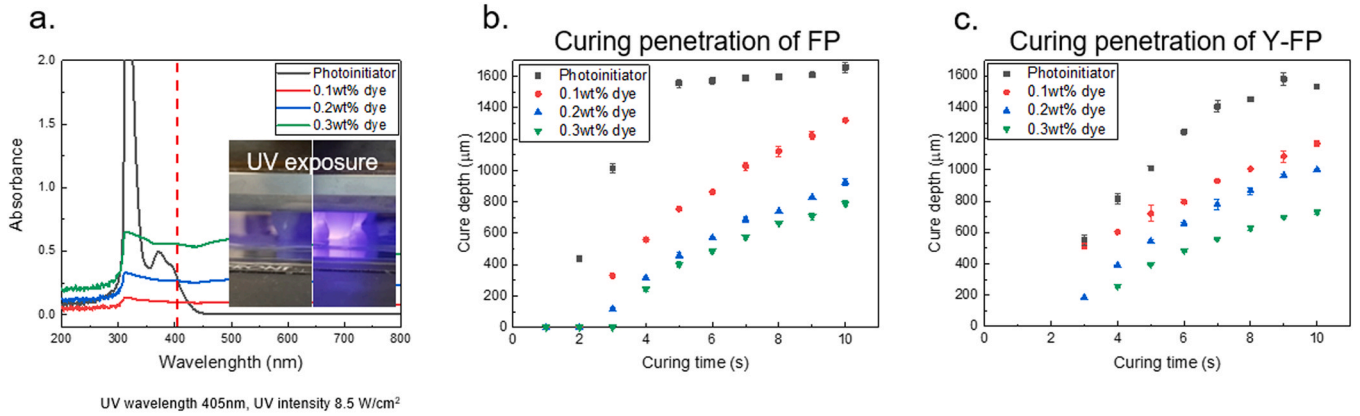

Fig. 3. - Curing behavior of FP slurry. (a) Comparison of UV absorbance between PI and RO16. (b) Curing penetration of FP slurry. (c) Curing penetration of Y-FP slurry.

3.2. UV sensitivity and curing penetration of slurry

We further examined UV sensitivity of the PI and RO16 dye in the FP slurry and the resultant curing penetration. In Fig. 3a, PI mainly absorbs UV light (black curve) in the range of 300–400 nm with peak absorbance on 320 and 380 nm. RO16 is used as an additive to improve the curing accuracy, and its optical absorbance is approximately constant at wavelengths longer than 300 nm and increases with its concentration in the slurry (red, blue, and green curves for 0.1, 0.2, and 0.3 wt%, respectively). Specifically, at the UV wavelength used in the fabrication equipment (405 nm), 0.2 wt% RO16 has the same absorbance as the PI.

Figs. 3b and 3c present the cure depths of FP and Y-FP slurries, respectively. After 2 s UV exposure, the basic FP slurry (with PI but no RO16) was cured to a depth of 439 μm, which increased greatly to 1600 μm when the exposure reached 5 s. The slurry containing 0.1 wt% added RO16 showed a shorter penetration depth (329 μm at 3 s, 1319 μm at 10 s). This trend of decreasing penetration continues for the slurries containing 0.2 and 0.3 wt% RO16, which had similar performance (minimum penetration depth: 115 and 244 μm, maximum: 923 and 787 μm at 10 s, respectively). In the Y-FP slurry, adding RO16 also reduced the curing penetration (minimum penetration depth: 185 and 257 μm, maximum: 1002 and 730 μm at 10 s, respectively). The only noticeable difference between the basic FP and basic Y-FP slurries is that the latter showed a moderate increase in penetration depth with prolonged exposure.

3.3. Structural accuracy assessment

Fig. 4 confirms that adding RO16 resulted in sharper shapes in the cured layer. When cured under a rectangular UV mask, sample layers

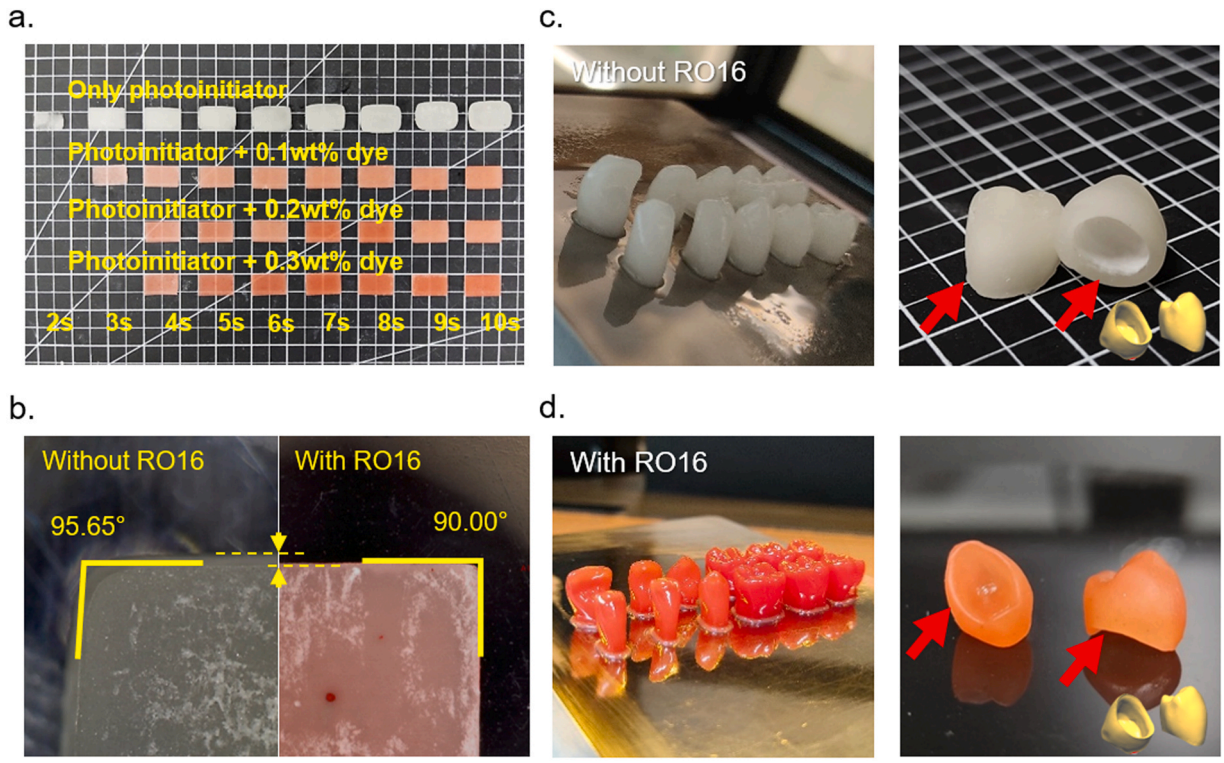

Fig. 4. - Curing accuracy of FP slurry. (a) Comparison of cured layers of FP slurry with various RO16 concentrations after prolonged UV exposure. (b) Comparison of angle formation between cured slurry layers without and with RO16. (c) Blurred details of samples fabricated with plain FP slurry. (d) Improved details of samples fabricated with RO16-added FP slurry.

Table 2
Measured density, linear shrinkage, and flexural bending strength of FP and Y-FP samples.

Type	Density (%)		Shrinkage at 780 °C (%)		Flexural bending strength (MPa)
	Debound	Sintered	X-Y axes	Z axis	
FP	71%	97%	21.66 ± 0.61	21.65 ± 0.31	106.29 ± 10.32
Y-FP			21.31 ± 0.45	21.59 ± 0.18	101.36 ± 7.32

with 0.1–0.3 wt% RO16 retained the rectangular shape with sharp angles, while those without RO16 displayed curved edges and rounded corners (Fig. 4a). According to Fig. 4b, at 4 s curing time, adding 0.2 wt % RO16 reduced the edge angle from 95.65° to 90°. The same improvement in edge thickness and shape was observed when the slurries were used to form full-scale teeth shapes (Fig. 4c vs. 4d).

3.4. Density, shrinkage, and flexural bending strength

All structures fabricated using slurries with 70 wt% solid loading showed comparable densities after debinding (71%), and their densities reached around 97% after particle solidification by sintering. Moreover, the measured shrinkage is similar between FP and Y-FP. The linear shrinkage was 21.6% both perpendicular and parallel to the fabrication direction. The flexural bending strength of sintered FP and Y-FP are also almost identical (106 and 101 MPa, respectively). The measured data are listed in Table 2.

3.5. CIELAB space and color difference

Fig. 5 shows photographs of the color-graded crowns. Crowns in the as-printed state (Fig. 5a) and just after debinding (Fig. 5b) have similar visual appearance because all of them are strongly tinted by RO16. However, color gradation becomes apparent after sintering (Fig. 5c).

Next, we quantitatively measured the color at nine sites on the model, three in each of the cervical, middle, and incisal regions (Fig. 6a). The obtained CIELAB coordinates are compared in Figs. 6b-6d. In Fig. 6b, all the L* values fall in a narrow range: 83.2–88.2 in the incisal region and 74.2–82 in the cervical region. As expected, crowns made using only FP and Y-FP showed constant hues. The FP crown is neutral between red and green ($a^* \approx 0.58$) and bluish between yellow and blue ($b^* = -3.15$), whereas the Y-FP crown is reddish ($a^* \approx 2.3$) and strongly yellow ($b^* = 14.8$). Next, we compared the a* and b* values in different segments for TYPE1–TYPE3 crowns with different compositions. For each type of crown, the a* and b* values decrease when moving from the cervical to the incisal region: 2.34–1.49 and 11.4–6.13 for TYPE1, 1.44–0.941 and 8.93–2.86 for TYPE2, and 0.464–0.079 and 7.16–1.21 for TYPE3, respectively.

Table 3 further compares the ΔE_{00} value between each segment and the single-color FP and Y-FP. The largest color difference was observed between the whitest (FP) and yellowest (Y-FP) samples (ΔE_{00} = 12.51–15.41). This value is generally smaller for the graded samples, whose colors should be intermediate between those of FP and Y-FP. TYPE1 is most similar in color to Y-FP, with ΔE_{00} = 2.11 (cervical), 2.36 (middle), and 7.27 (incisal). TYPE2 shows a more pronounced increase in ΔE_{00} with respect to Y-FP when moving from the cervical to the incisal region (ΔE_{00} = 2.84, 4.81, and 10.53, respectively). Finally, TYPE3 shows a greater color difference from Y-FP (4.43, 7.06, and 11.87, respectively).

4. Discussion

Properties of the ceramic slurry are a crucial factor during the first stage of fabrication process using the DLP system. The slurry must possess the appropriate viscosity and flowability for successful transfer from the feed container to the building platform, while it should also maintain stability during the standstill state to allow selective curing. These factors are essential to ensure a steady fabrication process. Moreover, particles with a narrow size distribution are preferred because they create a homogeneous and consistently stable ceramic slurry [45]. Dispersants can further improve the viscosity [46] and the capacity to incorporate solids. Our results indicated that 1 or 2 wt% BYK180 is insufficient to coat the FP particles, while 3 wt% of it could optimally encapsulated the particles as evidenced by the lowest slurry viscosity. On the other hand, excess BYK180 increases the hydrophobicity and causes flocculation due to van der Waals forces [43].

Unexpectedly, dispersion of the ceramic slurry is sustained due to a phenomenon in the film-based DLP system. Film movement during operation drags the slurry on top of it in the same direction. At the end, the slurry is forced to pass through a thin gap, while the excess slurry collides with the blade wall and is folded back in. This additional mixing reduces sedimentation that occurs during the stationary stage of

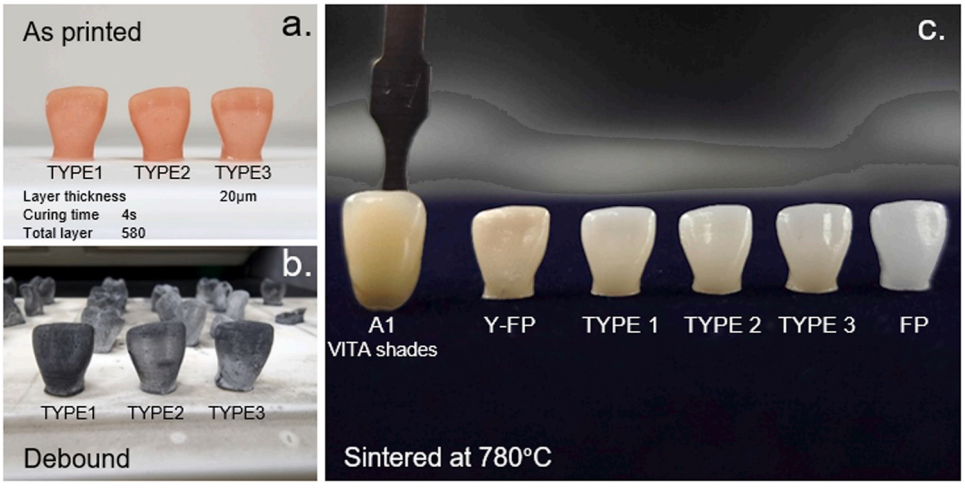

Fig. 5. - Crowns with color gradation fabricated with Y-FP/FP using FGAM. (a) Green body, (b) debound structure, (c) sintered structure with color gradation utilizing the anterior teeth model.

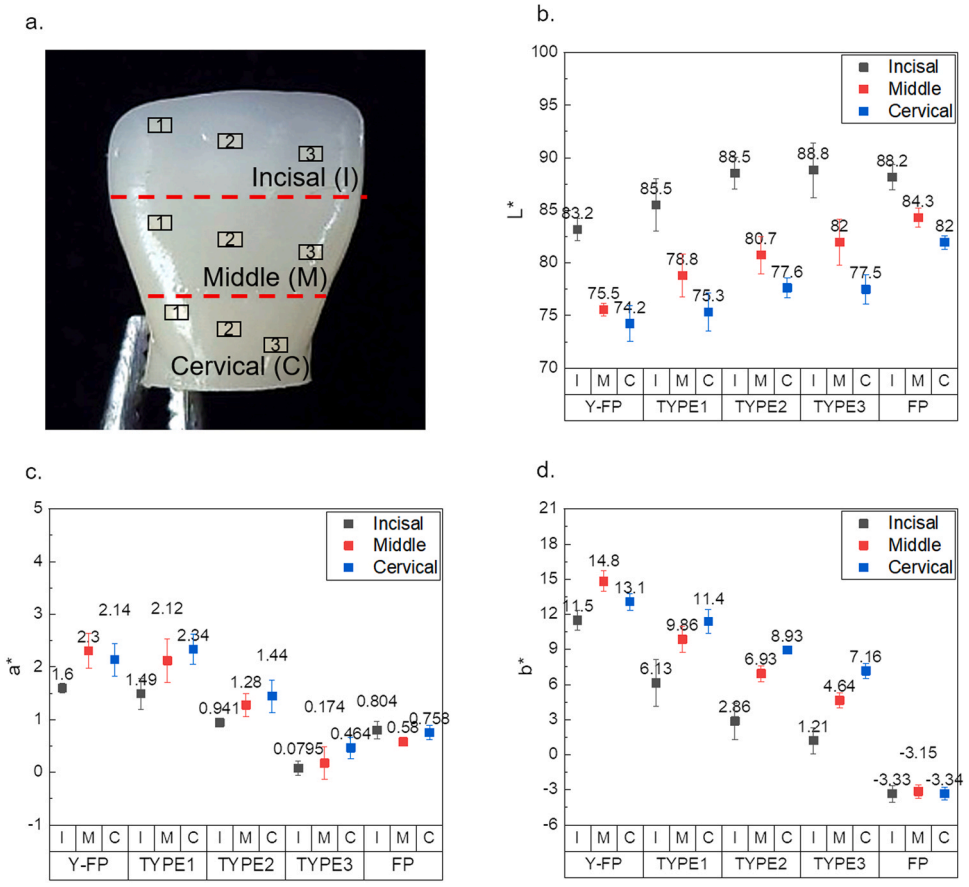

Fig. 6. - Comparison of CIELAB coordinates for Y-FP, TYPE1 gradation, TYPE2 gradation, TYPE3 gradation, and FP crowns. (a) Color sampling sites, (b) L* value, (c) a* value, (d) b* value.

Table 3
Comparison of color parameters of crowns fabricated using FP, TYPE1 gradation, TYPE2 gradation, TYPE 3 gradation, and Y-FP.

ΔE_{00}		μFP	μY-FP
FP	I		15.22
	M		14.07
	C		13.81
TYPE1	I	12.51	7.27
	M	15.92	2.36
	C	15.41	2.11
TYPE2	I	6.22	10.53
	M	9.65	4.81
	C	11.83	2.84
TYPE3	I	5.03	11.87
	M	7.74	7.06
	C	10.77	4.43
Y-FP	I	12.51	
	M	15.92	
	C	15.41	

* μFP/Y-FP: mean of the measured L* , a* , and b* values for FP and Y-FP
*Regions: incisal (I), middle (M), and cervical (C)

layer curing and during movement of the building platform.

After ascertaining the narrow particle size distribution and optimizing the amount of added BYK, we measured the viscosity at different solid loadings. The maximum solid loading could enhance the structural density and mechanical properties while maintaining slurry flowability (Fig. S2). We found that a 70 wt% solid loading was ideal, while a 75 wt % loading resulted in a highly viscous slurry (5 Pa·s and higher as the shear rate increased) that was difficult to transfer. Other researchers observed similarly viscous slurries at 3–5 Pa·s [47]. Conversely, an extremely low viscosity is also detrimental to the process. When the solid loading is very low, there are fewer particles to reduce the surface tension of the resin, and the resultant puddling phenomenon disrupts the thin slurry layer produced from the doctor blade.

Under UV irradiation, both FP and Y-FP slurries showed an extended curing depth due to the scattering of UV light after hitting the amorphous SiO_2 matrix [48]. The FP slurry was cured after only 2 s UV exposure, but the cured part was still weak and could be easily torn by motions during fabrication. Therefore, a minimum of 3 s UV exposure was needed to ensure successful curing of both FP and Y-FP slurries. Also, the FP slurry showed a deeper curing penetration compared to the Y-FP slurry (1013 vs. 550 μm), causing disparity in the fabrication parameters. This phenomenon is closely related to the small amount of YAG:Ce that hinders UV transmission. YAG:Ce usually has a high transmittance, but this value could be quite low in the amorphous phase prepared at temperatures below 800 °C [38]. Considering this characteristic, using thicker layers during printing (50 instead of 20 μm) could accelerate the processing at the price of reduced structural accuracy (Fig. 4c). Regardless, this curing behavior is undesirable because a significant amount of transmitted UV light is reflected from the fabrication target area to the surroundings to trigger excess curing reaction. Therefore, we introduced RO16 to inhibit the excess reaction that could obscure the structural details. This inhibition effect was accidentally discovered during the colored resin printing test. RO16 is an azo dye commonly used in the textile industry [49,50]. Some researchers employed it as a representative substrate for testing photocatalytic degradation [51,52], but we are unaware of any attempt to exploit it in the context of AM. The absorption range of RO16 (λ > 300 nm) overlaps with the PI absorption peak, and therefore RO16 can counter exorbitant UV absorption. Experimentally, we found that adding 0.2 wt% RO16 does not interfere with the ability of PI to initiate the curing reaction while decreasing unnecessary reactions

caused by the deflected UV light. As a result, the curing reaction strictly follows the shape of UV exposure and maintains shape accuracy during fabrication. Meanwhile, 0.3 wt% RO16 slightly improves the inhibition reaction at the cost of a longer minimum curing time.

After confirming successful structural fabrication, we identified the optimal processing temperatures, initial shrinkage points, and final linear shrinkage for both FP and Y-FP. This information is vital for processing multi-compositional structures. The debinding process was performed under nitrogen instead of open air environment to ensure a steady heat flow. This allows the degradation of organic compounds to proceed under more stable conditions, preventing possible cracking on the green body due to a surging reaction. A heating sequence was then proposed based on the TG/DSC data (Fig. S3a). The first holding point (300 °C) was determined by the starting of weight loss, in order to homogenize the temperature throughout the green body before degradation reaction occurs. The second and third holding points (350 and 400 °C) represent the anticipated temperatures of binder burnout reaction. Lastly, additional soaking was performed at 650 °C to ensure complete reaction. The heating rate in the process was the same as that used in thermal analysis (1 °C/min), whereas heating in the final step (400–650 °C) occurred at a faster rate of 5 °C/min because the majority of reactions had already occurred. The furnace heating sequence is depicted in Fig. S3b. After this procedure, the sample density (71%) was very similar to the solid loading in the starting slurry. Eventually, the debound green body was subjected to another sintering process at 780 °C (glass transition temperature, Tg), where the heat flow fluctuates to consolidate the structure into a solid body (Fig. S3c). This Tg value is considerably lower than those of conventional feldspathic glass materials [53] due to the addition of Na_2O [54]. We chose this to be the sintering temperature, because even a slightly higher temperature resulted in notable structural distortion while a lower temperature produced a rougher surface. Unfortunately, complete removal of organic compounds is unattainable in practice. Hence, the samples were held for another 3 h at 300 °C during sintering to further remove the organic residue, before holding it again at Tg for 3 h (Fig. S3d).

The initial shrinkage was further checked using dilatometry (Fig. S3e). Fortunately, the addition of YAG:Ce in Y-FP did not affect the initial shrinkage behavior, as both FP and Y-FP began to shrink at approximately 630 °C. The final shrinkage was ignored in this analysis, because that step was performed only up to 700 °C instead of 780 °C to avoid major sample distortions that might impair the equipment. As a result of the identical initial and final linear shrinkages between FP and Y-FP, we could easily apply compositional gradation without adjusting the thermal treatment.

The flexural bending strength of sintered structures is comparable to that of typical block leucite-reinforced porcelain used commercially [55,56], even though the sintering temperature is relatively lower than general feldspathic glass. This highlights the practicality of AM-fabricated FP as a Class 2 dental ceramic suitable for single-unit anterior or posterior adhesively cemented crowns (ADA 69/ISO 6872:2015 [57]). Note that the strength might be further improved by controlling the particle size to less than 1 μm [54,56,58].

Finally, crowns mimicking the color gradation of natural teeth were fabricated using slurries with 70 wt% solid loading, 3 wt% BYK180, 0.2 wt% RO16, and FP/Y-FP in various compositions shown in Table 1. Prior to sintering, the bright orange color of RO16 obscured the color difference between different compositions within the same sample. In the sintered crowns, the cervical and middle regions of TYPE1 are indistinguishable in color from Y-FP (based on an oral ambiance color tolerance of $\Delta E < 3.7$ [59]), with slightly lighter colors in the incisal region. TYPE2 shows a larger ΔE_{00} from Y-FP in the cervical region and becomes gradually brighter in the middle and incisal regions, although the color in its incisal region still does not match that of FP. A similar trend was observed for TYPE3. The color of its middle and incisal regions are similar to FP, with moderate ΔE_{00} values of 7.74 and 5.03, respectively. Indeed, it is expected that ΔE_{00} toward FP will decrease from cervical to incisal region and vice versa towards Y-FP, but these results show disparate gradation to the model intention. Furthermore, there is no noticeable lining between segments with different compositions (Figs. 5c and 6a) as compared to pressed multilayer zirconia with Fe_2O_3 color gradient [13] and multilayer pre-colored zirconia (anterior multilayer, ATM) fabricated by Aidite Technology [60]. Self-diffusion likely occurred during sintering at Tg [61], during which the YAG:Ce particles moved to an area with low concentrations of them. Moreover, the glassy surface of porcelain made it difficult to observe the line of composition change. Consequently, this aspect needs to be considered during the color modeling process.

Here, we used a mobile phone camera for color measurement due to the contour and color transition of the crown structure. Common spectrophotometers and colorimeters require a minimum measurement area of 3–5 mm in size [66], whereas much smaller areas or points should be measured when investigating color gradation. Digital photography can easily capture color change on an uneven surface and output the color values of single pixels. Future studies should compare results obtained using spectrophotometers, digital cameras, and mobile phone cameras. For example, one source reported $\Delta E < 6.8$ [62] while others considered $\Delta E = 3.4$ acceptable [63]. Although mobile phone cameras using the default setting are less accurate than digital cameras [63,64], another study obtained identical color measurements with a visual method in a simulated clinic scenario [65]. To minimize inconsistent results, in this study we further fixed the camera exposure, shutter, white balance, and lighting parameters [66], and the photographs were taken in a closed booth with a dark background.

5. Conclusion

This study aimed at fabricating dental crowns with color gradation using the FGAM process. The optimal ceramic slurry was found to contain 70 wt% solids (FP or Y-FP) plus 3 wt% BYK180 to ensure good flowability during the fabrication process. Because both FP and Y-FP showed higher curability than expected, 0.2 wt% RO16 was added to offset the overcuring. Overall, the fabricated crown structures satisfy requirements for Class 2 dental prosthetics (ADA69/ISO 6872:2015), with the flexural bending strengths of 106.23 MPa for FP and 101.36 MPa for Y-FP. Smooth color gradation was successfully produced on the crown, demonstrating feasibility of the FGAM process. However, further analysis in color modeling is required because of the self-diffusion of YAG:Ce colorant.

Acknowledgments

This work was supported by the Fundamental Research Program of the Korea Institute of Material Science (PNK8850).

Appendix A. Supporting information

Supplementary data associated with this article can be found in the online version at doi:10.1016/j.dental.2023.03.021.

References

[1] AL-Omiri MK, Karasneh JA, Lynch E, Lamey P-J, Clifford TJ. Impacts of missing upper anterior teeth on daly living. Int Dent J 2008;59:127–32. https://doi.org/10.1922/IDJ

[2] Leao A, Sheiham A. The development of a socio-dental measure of dental impacts on daily living. Community Dent Health 1996;13:22–6.

[3] Rodríguez-López S, Escobedo Martínez MF, García-Pola M, Junquera LM. Analysis of the esthetic preferences of Spanish laypersons and dentists regarding the different width proportions of the maxillary anterior teeth. J Prosthet Dent 2021:1–9. https://doi.org/10.1016/j.prosdent.2021.06.041

[4] Tavarez RRDJ, Lima SNL, Malheiros AS, Menezes LL, Bandeca MC, de Miranda RDCM, et al. Assessment of the aesthetic impact and quality of life of home dental bleaching in adult patients. J Clin Exp Dent 2021;13:440–5. https://doi.org/10.4317/jced.57831

[5] Dos Santos DM, Moreno A, Vechiato-Filho AJ, Da Rocha Bonatto L, Pesqueira AA,

Laurindo MCB, et al. The importance of the lifelike esthetic appearance of all-ceramic restorations on anterior teeth. Case Rep Dent 2015:2015. https://doi.org/10.1155/2015/704348
[6] Nuzzolese E, Lepore MM, Cukovic-Bagic I, Vella FM, Di G. Forensic sciences and forensic odontology. Int Dent J 2008;58:342–8. https://doi.org/10.1922/IDJ
[7] Kamishima N, Ikeda T, Sano H. Color and translucency of resin composites for layering. Techniques 2005;24:428–32.
[8] Rocha Maia R, Oliveira D, D'Antonio T, Qian F, Skiff F. Comparison of light-transmittance in dental tissues and dental composite restorations using incremental layering build-up with varying enamel resin layer thickness. Restor Dent Endod 2018;43:1–9. https://doi.org/10.5395/rde.2018.43.e22
[9] Da Costa J, Fox P, Ferracane J. Comparison of various resin composite shades and layering technique with a shade guide. J Esthet Restor Dent 2010;22:114–24. https://doi.org/10.1111/j.1708-8240.2010.00322.x
[10] Roozen S. The color gradient of natural teeth and their intelligent imitation. Int Dent Afr Ed 2021;11. 62:8.
[11] Kaizer MR, Kolakarnprasert N, Rodrigues C, Chai H, Zhang Y. Probing the interfacial strength of novel multi-layer zirconias. Dent Mater 2020;36:60–7. https://doi.org/10.1016/j.dental.2019.10.008
[12] Li X, Wang Q, Qiu X, Zhao B. Effect of different CAD/CAM cutting depths on the post-fatigue load-bearing capacity of novel multilayer zirconia restorations. J Dent 2021;111:103709https://doi.org/10.1016/j.jdent.2021.103709
[13] Alves MFRP, Abreu LG, Klippel GGP, Santos C, Strecker K. Mechanical properties and translucency of a multi-layered zirconia with color gradient for dental applications. Ceram Int 2021;47:301–9. https://doi.org/10.1016/j.ceramint.2020.08.134
[14] Kang CM, Peng TY, Shimoe S. Color accuracy of different types of monolithic multilayer precolored zirconia ceramics. J Prosthet Dent 2020;124:789.e1–7. https://doi.org/10.1016/j.prosdent.2020.04.026
[15] Oliveira TT, Reis AC. Fabrication of dental implants by the additive manufacturing method: a systematic review. J Prosthet Dent 2019;122:270–4. https://doi.org/10.1016/j.prosdent.2019.01.018
[16] Jockusch J, Özcan M. Additive manufacturing of dental polymers: an overview on processes materials and applications. Dent Mater J 2020;39:345–54. https://doi.org/10.4012/dmj.2019-123
[17] Javaid M, Haleem A. Current status and applications of additive manufacturing in dentistry: a literature-based review. J Oral Biol Craniofacial Res 2019;9:179–85. https://doi.org/10.1016/j.jobcr.2019.04.004
[18] Galante R, Figueiredo-Pina CG, Serro AP. Additive manufacturing of ceramics for dental applications: a review. Dent Mater 2019;35:825–46. https://doi.org/10.1016/j.dental.2019.02.026
[19] Anssari Moin D, Hassan B, Wismeijer D. A novel approach for custom three-dimensional printing of a zirconia root analogue implant by digital light processing. Clin Oral Implants Res 2017;28:668–70. https://doi.org/10.1111/clr.12859
[20] Li H, Song L, Sun J, Ma J, Shen Z. Dental ceramic prostheses by stereolithography-based additive manufacturing: potentials and challenges. Adv Appl Ceram 2019;118:30–6. https://doi.org/10.1080/17436753.2018.1447834
[21] Dehurtevent M, Robberecht L, Hornez JC, Thuault A, Deveaux E, Béhin P. Stereolithography: a new method for processing dental ceramics by additive computer-aided manufacturing. Dent Mater 2017;33:477–85. https://doi.org/10.1016/j.dental.2017.01.018
[22] Baumgartner S, Gmeiner R, Schönherr JA, Stampfl J. Stereolithography-based additive manufacturing of lithium disilicate glass ceramic for dental applications. Mater Sci Eng C Mater Biol Appl 2020;116:111180https://doi.org/10.1016/j.msec.2020.111180
[23] Schweiger J, Bomze D, Schwentenwein M. 3D printing of zirconia–what is the future? Curr Oral Heal Rep 2019;6:339–43. https://doi.org/10.1007/s40496-019-00243-4
[24] Wang L, Yao L, Tang W, Dou R. Effect of Fe2O3 doping on color and mechanical properties of dental 3Y-TZP ceramics fabricated by stereolithography-based additive manufacturing. Ceram Int 2022:1–11. https://doi.org/10.1016/j.ceramint.2022.12.062
[25] Loh GH, Pei E, Harrison D, Monzón MD. An overview of functionally graded additive manufacturing. Addit Manuf 2018;23:34–44. https://doi.org/10.1016/j.addma.2018.06.023
[26] Gonzalez P, Schwarzer E, Scheithauer U, Kooijmans N, Moritz T. Additive manufacturing of functionally graded ceramic materials by stereolithography. J Vis Exp 2019;2019:1–8. https://doi.org/10.3791/57943
[27] Oxman N, Keating S, Tsai E. Functionally graded rapid prototyping. Innov Dev Virtual Phys Prototyp - Proc 5th Int Conf Adv Res Rapid Prototyp 2012:483–9. https://doi.org/10.1201/b11341-78
[28] Denry I, Holloway JA. Ceramics for dental applications: a review. Materials 2010;3:351–68. https://doi.org/10.3390/ma3010351
[29] Moshaverinia A. Review of the modern dental ceramic restorative materials for esthetic dentistry in the minimally invasive age. Dent Clin North Am 2020;64:621–31. https://doi.org/10.1016/j.cden.2020.05.002
[30] Chu SJ, Devigus A, Paravina RD, Mieleszko AJ. Fundamentals of Color: Shade Matching and Communication in Esthetic Dentistry. Second edi.., Quintessence Publishing Co, Inc,; 2011.
[31] Santander SA, Vargas AP, Escobar JS, Monteiro FJ, Tamayo LFR. Ceramics for dental restorations - an introduction. DYNA 2010;77:26–36.
[32] Osilo G. Flexural strength and internal defects of some dental porcelains. Acta Odontol Scand 1988;46:313–22. https://doi.org/10.3109/00016358809004782
[33] Ardlin BI. Transformation-toughened zirconia for dental inlays crowns and bridges: chemical stability and effect of low-temperature aging on flexural strength and surface structure. Dent Mater 2002;18:590–5. https://doi.org/10.1016/S0109-5641(01)00095-1
[34] Shah K, Holloway JA, Denry IL. Effect of coloring with various metal oxides on the microstructure color and flexural strength of 3Y-TZP. J Biomed Mater Res Part B Appl Biomater 2008;87:329–37. https://doi.org/10.1002/jbm.b.31107
[35] Khabas TA, Klimova VV, Starosvetskiy SI, Vasilyeva AP, Zvigintsev MA. Crystal phase formation in colored leucite-reinforced glass-ceramics for dental restorations. Inorg Mater Appl Res 2017;8:186–93. https://doi.org/10.1134/S2075113317010191
[36] Baran GR, O'brien WJ, Tien TY. Colored emission of rare earth ions in a potassium feldspar glass. J Dent Res 1977;56:1323–9. https://doi.org/10.1177/00220345770560110401
[37] Geusic JE, Marcos HM, Van Uitert LG. Laser oscillations in nd-doped yttrium aluminum yttrium gallium and gadolinium garnets. Appl Phys Lett 1964;4:182–4. https://doi.org/10.1063/1.1753928
[38] Michálková M, Kraxner J, Michálek M, Galusek D. Preparation of translucent YAG glass/ceramic at temperatures below 900 °C. J Eur Ceram Soc 2020;40:2581–5. https://doi.org/10.1016/j.jeurceramsoc.2019.11.011
[39] Kostić S, Lazarević Z, Radojević V, Milutinović A, Romčević M, Romčević N, et al. Study of structural and optical properties of YAG and Nd:YAG single crystals. Mater Res Bull 2015;63:80–7. https://doi.org/10.1016/j.materresbull.2014.11.033
[40] Komissarenko D, Sokolov P, Evstigneeva A, Shmeleva I, Dosovitsky A. Rheological and curing behavior of acrylate-based suspensions for the dlp 3d printing of complex zirconia parts. Materials 2018;11:2350. https://doi.org/10.3390/ma11122350
[41] Mitteramskogler G, Gmeiner R, Felzmann R, Gruber S, Hofstetter C, Stampfl J, et al. Light curing strategies for lithography-based additive manufacturing of customized ceramics. Addit Manuf 2014;1:110–8. https://doi.org/10.1016/j.addma.2014.08.003
[42] Zhang S, Sutejo IA, Kim J, Choi Y, Park H, Yun HH. Three-dimensional complex construct fabrication of illite by digital light processing-based additive manufacturing technology. J Am Ceram Soc 2022;105:3827–37. https://doi.org/10.1111/jace.18369
[43] Kim J, Choi YJ, Gal CW, Park H, Yoon SY, Yun H suk. Effect of dispersants on structural integrity of 3D printed ceramics. Int J Appl Ceram Technol 2022;19:968–78. https://doi.org/10.1111/ijac.13965
[44] Sharma G, Wu W, Dalal EN. The CIEDE2000 color-difference formula: implementation notes supplementary test data and mathematical observations. Color Res Appl 2005;30:21–30. https://doi.org/10.1002/col.20070
[45] Zhang S, Sutejo IA, Kim J, Choi Y, Gal CW, Yun HS. Fabrication of complex three-dimensional structures of mica through digital light processing-based additive manufacturing. Ceramics 2022;5:562–74. https://doi.org/10.3390/ceramics5030042
[46] Chen F, Wu YR, Wu JM, Zhu H, Chen S, Hua SBin, et al. Preparation and characterization of ZrO2-Al2O3 bioceramics by stereolithography technology for dental restorations. Addit Manuf 2021;44:1–8. https://doi.org/10.1016/j.addma.2021.102055
[47] Inserra B, Coppola B, Montanaro L, Tulliani JM, Palmero P. Preparation and characterization of Ce-ZrO2/Al2O3 composites by DLP-based stereolithography. J Eur Ceram Soc 2022;43:2907–16. https://doi.org/10.1016/j.jeurceramsoc.2022.08.037
[48] Lazauskas A, Jucius D, Puodžiukynas L, Guobienė A, Grigaliūnas V. Sio2-based nanostructured superhydrophobic film with high optical transmittance. Coatings 2020;10:1–7. https://doi.org/10.3390/coatings10100934
[49] Sukhdev A, Manjunatha AS, Puttaswamy. Decolorization of reactive orange 16 azo dye in wastewater using CAT/ IrCl3/HClO4 redox system: delineation of kinetic modeling and mechanistic approaches. J Taiwan Inst Chem Eng 2017;70:150–60. https://doi.org/10.1016/j.jtice.2016.10.033
[50] Benkhaya S, M'rabet S, El Harfi A. Classifications properties recent synthesis and applications of azo dyes. Heliyon 2020:6. https://doi.org/10.1016/j.heliyon.2020.e03271
[51] Yildiz T, Yatmaz HC, Öztürk K. Anatase TiO2 powder immobilized on reticulated Al2O3 ceramics as a photocatalyst for degradation of RO16 azo dye. Ceram Int 2020;46:8651–7. https://doi.org/10.1016/j.ceramint.2019.12.098
[52] Arfin T, Bhaisare DA, Waghmare SS. Development of a PANI/Fe(NO3)2nanomaterial for reactive orange 16 (RO16) dye removal. Anal Methods 2021;13:5309–27. https://doi.org/10.1039/d1ay01402a
[53] Sheu TS, O'Brien WJ, Rasmussen ST, Tien TY. Mechanical properties and thermal expansion behaviour in leucite containing materials. J Mater Sci 1994;29:125–8. https://doi.org/10.1007/BF00356582
[54] Saint-Jean SJ. Dental Glasses and Glass-ceramics. Elsevier Inc,; 2014. https://doi.org/10.1016/B978-0-12-394619-5.00012-2
[55] Tanaka CB, Ahmad NHB, Ellakwa A, Kruzic JJ. Effect of cooling protocol on mechanical properties and microstructure of dental veneering ceramics. Dent Mater 2019;35:1498–505. https://doi.org/10.1016/j.dental.2019.07.011
[56] Zhang Y, Rao P, Lü M, Wu J. Mechanical properties of dental porcelain with different leucite particle sizes. J Am Ceram Soc 2008;91:527–34. https://doi.org/10.1111/j.1551-2916.2007.02179.x
[57] International Organization for Standardization. Dentistry – Ceramic materials (ISO Standard No. 6872). 4th ed. 2015.
[58] Chen X, Chadwick TC, Wilson RM, Hill R, Cattell MJ. Crystallization of high-strength fine-sized leucite glass-ceramics. J Dent Res 2010;89:1510–6. https://doi.org/10.1177/0022034510377795
[59] Johnston WM, Kao EC. Assessment of appearance match by visual observation and clinical colorimetry. J Dent Res 1989;68(5):819–22. 819.
[60] Kang CM, Peng TY, Huang HH. Effects of thickness of different types of high-translucency monolithic multilayer precolored zirconia on color accuracy: an in vitro study. J Prosthet Dent 2021;126:587.e1–8. https://doi.org/10.1016/j.

prosdent.2021.07.011
[61] Nascimento MLF, Zanotto ED. Mechanisms and dynamics of crystal growth viscous flow and self-diffusion in silica glass. Phys Rev B Condens Matter Mater Phys 2006;73:1–7. https://doi.org/10.1103/PhysRevB.73.024209
[62] Mahn E, Tortora SC, Olate B, Cacciuttolo F, Kernitsky J, Jorquera G. Comparison of visual analog shade matching a digital visual method with a cross-polarized light filter and a spectrophotometer for dental color matching. J Prosthet Dent 2021;125:511–6. https://doi.org/10.1016/j.prosdent.2020.02.002
[63] Sampaio CS, Atria PJ, Hirata R, Jorquera G. Variability of color matching with different digital photography techniques and a gray reference card. J Prosthet Dent 2019;121:333–9. https://doi.org/10.1016/j.prosdent.2018.03.009
[64] Saincher R, Kumar S, Gopalkrishna P, Maithri M, Sherigar P. Comparison of color accuracy and picture quality of digital SLR point and shoot and mobile cameras used for dental intraoral photography - a pilot study. Heliyon 2022;8:e09262https://doi.org/10.1016/j.heliyon.2022.e09262
[65] Schropp L. Shade matching assisted by digital photography and computer software. J Prosthodont 2009;18:235–41. https://doi.org/10.1111/j.1532-849X.2008.00409.x
[66] Wagner DJ. A beginning guide for dental photography: a simplified introduction for esthetic dentistry. Dent Clin North Am 2020;64:669–96. https://doi.org/10.1016/j.cden.2020.07.002